Nanoscale

PAPER

View Article Online
View Journal | View Issue



Cite this: *Nanoscale*, 2026, **18**, 2585

# Nitrilotriacetic acid functionalized gold nanopillars enable stochastic detection and deep learning analysis of prolines and hydroxyprolines by surface enhanced Raman spectroscopy

Yuan Zhang,[a] Kuo Zhan,[a,b] Peilin Xin,[a,b] Yingqi Zhao,[a,b] Ibrar Alam,[a] Shubo Wang,[d] Aliaksandr Hubarevich,[e] Kai Liu,[f] Xuejin Zhang[f] and Jianan Huang *[a,b,c]

Proline hydroxylation is crucial for monitoring diseases related to collagen metabolism, analyzing metabolic pathways, and evaluating therapeutic or nutritional outcomes. However, the small differences in the hydroxyl group between prolines (Pro) and hydroxyprolines (Hyp) are challenging for reliable label-free discrimination by surface-enhanced Raman scattering (SERS) based on silver and gold nanoparticles. Adsorption of Pro and Hyp on metal colloids took 72 and 48 hours, respectively, which led to occupation of the colloid surface by Hyp and thus overlapping SERS signals of Hyp against those of Pro. Here, we developed a stochastic SERS method to detect prolines and hydroxyprolines within 30 minutes by functionalizing gold nanopillars with nitrilotriacetic acid (NTA) and nickel ions ($Ni^{2+}$) to form the NTA–Ni structure for reversible and transient binding of Pro/Hyp. By analyzing the SERS time series of NTA–Ni–Pro/Hyp using the event occurrence frequency, we extracted their SERS feature for the study of binding kinetics and quantification with the detection limits down to 0.20 nM for Pro and 0.23 nM for Hyp in mixture. To overcome the signal fluctuation, we developed a one-dimensional convolutional neural network model to identify NTA–Ni–Pro and NTA–Ni–Hyp with high accuracies of 86.9% and 89.6%, respectively. Our study demonstrated a new SERS strategy of hydroxylation detection by combining stochastic sensing and deep learning analysis. The excellent practicality of our method is promising for binding and analyzing post-translational modifications in biofluids for biomedical complex quantitative analysis and early diagnosis of diseases.

Received 29th September 2025,
Accepted 19th December 2025

DOI: 10.1039/d5nr04125b

rsc.li/nanoscale



## 1. Introduction

Proline (Pro) is an important proteinogenic amino acid, which has an exceptional structure and is fundamental for many metabolic processes.[1] Hydroxyproline (Hyp) is a non-essential amino acid derived from Pro through an oxygen sensing post-translational modification regulated tumor cell metastasis.[2–7] The modification occurs by prolyl hydroxylases that add a single hydroxyl group (–OH) to replace the hydrogen of the Pro pyrrolidine ring. Hyp can subtly influence the protein structures, activities, and properties of protein–protein interactions in the cell and play a pivotal role in cancer development and disease progression.[8] Therefore, distinguishing Hyp from Pro is crucial to studying the collagen structure, monitoring diseases related to collagen metabolism, analyzing metabolic pathways, and evaluating therapeutic or nutritional outcomes.[9,10]

Current methods for the detection of Pro and Hyp have limitations. The isatin paper assays based on the reaction between isatin and proline to form pyrrole blue are simple but not sensitive.[11] Colorimetric techniques, such as ninhydrin reactions, are reliable but are influenced by reaction variability.[12] High-performance liquid chromatography (HPLC) provides detailed amino acid profiles but is costly and time intensive.[13] Mass spectrometry offers high sensitivity and detailed modifications but requires expertise and expensive equipment.[14] Alternatively, surface-enhanced Raman spectroscopy (SERS) is promising for the detection of Pro and Hyp because it combines the molecular specificity of vibrational Raman

[a]*Research Unit of Health Sciences and Technology (HST), Faculty of Medicine, University of Oulu, Oulu 90220, Finland. E-mail: jianan.huang@oulu.fi*
[b]*Biocenter Oulu, University of Oulu, Oulu 90220, Finland*
[c]*Research Unit of Disease Networks, Faculty of Biochemistry and Molecular Medicine, University of Oulu, Oulu 90220, Finland*
[d]*Nano and Molecular Systems Research Unit, Faculty of Science, University of Oulu, Oulu 90570, Finland*
[e]*Plasmon Nanotechology Unit, Istituto Italiano di Tecnologia, Via Morego 30, 16163 Genova, Italy*
[f]*School of Physics and College of Engineering and Applied Sciences, Nanjing University, Nanjing 210093, China*

spectroscopy with high sensitivity to provide rich fingerprint information of analytes.

However, the small differences in the molecular structure (–OH group with 17.01 Da) between Hyp and Pro are challenging for reproducible SERS detection of Pro and Hyp, which requires prolonged physical adsorption of the analytes on metal colloids.[15–17] For example, J. J. Cárcamo *et al.*[15] prepared silver colloids at a controlled and fixed pH, allowing the analyte to be physically adsorbed on the colloid surface to obtain unique and reproducible SERS spectra. Accordingly, the required adsorption times for Pro and Hyp in the silver colloids for distinguishable and reproducible SERS spectra were 72 hours for Pro and 48 hours for Hyp. Similarly, our recent single-molecule SERS sensor employed gold colloids to distinguish SERS spectra of Hyp and Pro, which needed a 48-hour incubation time to absorb the Hyp or Pro on the gold nanoparticles.[16] These works implied that physical adsorption would be difficult for practical SERS detection of mixtures of Hyp and Pro in biofluids due to their long adsorption time.

To decrease the detection time, an effective receptor is explored to uniquely bind both analytes on plasmonic nanostructures. One such trial was functionalized silver colloids with a covalent organic framework with carboxylate groups (Ag@COF–COOH) to capture the Hyp based on the hydrogen-binding mechanism for SERS detection.[18] The detection time (10–15 minutes) was much shorter than that of analyte adsorption on colloids, which was then used in fast Hyp detection in milk complex. However, the authors did not demonstrate SERS detection of Pro. Meanwhile, the Ag@COF–COOH binding probability is the same for both Hyp and Pro, which means that it cannot distinguish Hyp from Pro. This example highlighted the challenge of unique binding of Pro and Hyp due to the small hydroxyl group between them and inspired us to design a new binding and analysis strategy for fast detection of Pro and Hyp.

In this study, we bound nitrilotriacetic acid (NTA) with nickel cations ($Ni^{2+}$) to form the NTA–Ni structure as the receptor on plasmonic gold nanopillars (AuNPs) for stochastic SERS detection of Pro and Hyp in liquid within 30 minutes as shown in Fig. 1a and b. The gold nanopillar has a stable wide-range hot spot (Fig. 1c and d) to cover the long molecule moieties for reproducible SERS detection.[19,20] The SERS time-series signals of the bound NTA–Ni–Pro and NTA–Ni–Hyp (Fig. 1e and f) were then analyzed and distinguished with a deep learning model.

Similar to that of histidine, the binding of Pro by NTA–Ni was reversible and stochastic through chelation. Due to the five-membered ring structure in the side chain of Pro, NTA–Ni binding to Pro was found to be 10 times longer than it is to other proteogenic amino acids.[21,22] Because of the similar molecular structure of Hyp and Pro, the resultant SERS time-series of NTA–Ni–Pro and NTA–Ni–Hyp would exhibit more Raman signals, or detection events, than those of other amino acids, which allows us to distinguish them by event frequency analysis.[17] Such a method is significantly different from other SERS sensors based on NTA–metal complexes that detected the analytes by the intensity of SERS bands. For example, Li *et al.* fabricated gold nanoparticle substrates modified with NTA–$Ni^{2+}$ complexes to capture histamine through the formation of NTA–$Ni^{2+}$–histamine coordination complexes.[23] The NTA–$Ni^{2+}$-decorated gold nanoparticle nanoprobe exhibited a detection sensitivity down to 1 μM for histamine. In another report, Kaya *et al.* employed AgNPs modified with NTA–$Fe^{3+}$ complexes as SERS-active substrates for dopamine detection, even in the presence of ascorbic acid.[24] In this case, the formation of NTA–$Fe^{3+}$–dopamine complexes significantly amplified the Raman response, enabling detection at the picomolar (pM) level. Likewise, Cao *et al.* demonstrated sensitive SERS analysis of catecholamines using polyvinylpyrrolidone-capped AuNPs functionalized with NTA–$Fe^{3+}$ complexes.[25]

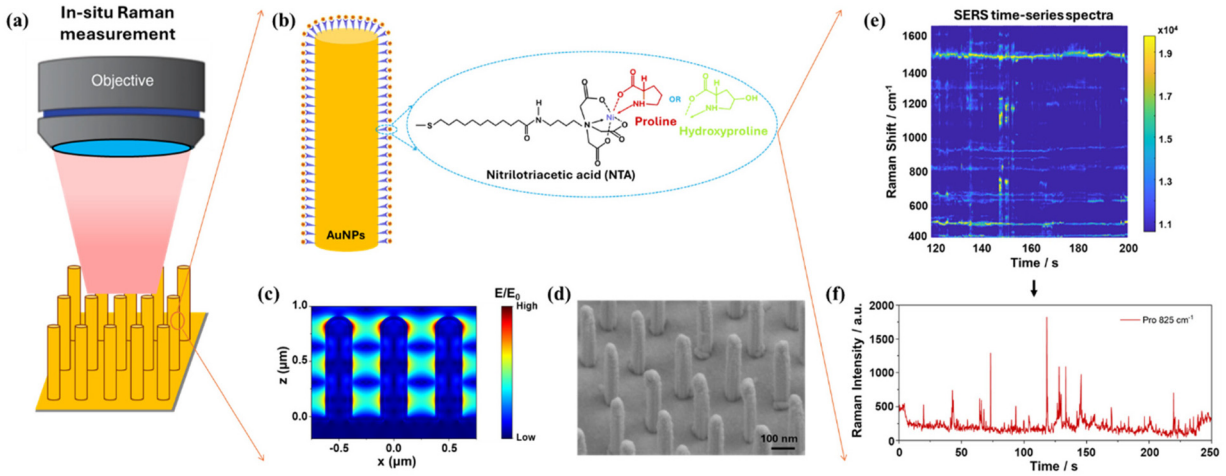


**Fig. 1** (a) *In situ* Raman measurement of Pro and Hyp. (b) Schematic of the stochastic binding of Pro and Hyp using the NTA–Ni bond on the AuNPs. (c) Simulated electric field intensity distribution of AuNPs at 785 nm. The color bar shows the enhancement of the electric field intensity. (d) SEM image of AuNPs. (e) The time-series SERS spectra of AuNP–NTA–Ni–Pro. The color bars show the intensities of SERS bands. (f) Corresponding SERS time trace after spectral processing of Pro.

The SERS time series signals of NTA–Ni–Pro and NTA–Ni–Hyp were still similar, which will be analyzed for the binding kinetics and quantification based on the event frequencies of these biomolecules. Finally, combining the deep learning analysis using the convolutional neural network model, our method has identified NTA–Ni–Pro and NTA–Ni–Hyp with more than 90% accuracy with a detection limit of 0.1 pM. To the best of our knowledge, this is the first successful quantitative and fast analysis of Pro and Hyp using NTA as the receptor, which is promising for binding and analyzing post-translational modifications in biofluids for rapid biomedical analysis and early diagnosis of diseases.

## 2. Experimental section

### Materials

Silicon wafers (prime CZ–Si wafer, 4-inch, thickness = 525 ± 25 μm, (111), 1-side polished, p-type (boron), TTV < 10 μm, 1–10 Ohm cm) were purchased from MicroChemicals GmbH; polystyrene nanospheres of 0.5 μm diameter were purchased from Micro Particles GmbH; ethanol ($CH_3CH_2OH$) of purity ≥99.8%, AnalaR NORMAPUR® ACS, analytical reagent, and nickel(II) chloride ($NiCl_2$) were purchased from Fisher Scientific; ethylene glycol ($HOCH_2CH_2OH$), acetone ($CH_3COCH_3$), sodium dodecyl sulfate solution (SDS, $CH_3(CH_2)_{11}OSO_3Na$), hydrogen peroxide solution ($H_2O_2$), hydrofluoric acid (HF), *N*-*N*α,*N*α-bis(carboxymethyl)-L-lysine-12-mercaptododecanamide (NTA, $C_{22}H_{40}N_2O_7S$), L-proline ($C_5H_9NO_2$), *trans*-4-hydroxy-L-proline ($C_5H_9NO_3$), cysteine ($C_3H_7NO_2S$), histidine ($C_6H_9N_3O_2$), and serine ($C_3H_7NO_3$) were purchased from Sigma-Aldrich.

### Gold nanopillar fabrication

The fabrication of gold coated silicon pillars was based on the established nanosphere lithography protocol.[19] The procedures follow these steps: firstly, depositing 500 nm polystyrene nanospheres on the surface of 1 × 1 cm silicon wafers. The silicon wafers were made hydrophilic using oxygen plasma (Gambetti Tecnologia Colibri and bench-top plasma system, Italy). An automatic pump was used to control the speed of the polystyrene sphere droplet, and when the polystyrene sphere fully occupied the Petri dish, the cleaned wafers were used to carry out the polystyrene sphere single layer. The wafers with polystyrene spheres were allowed to naturally dry; then a reactive ion etching instrument (RIE, Oxford Instruments PlasmaLab 80 Plus PECVD/ICP-DRIE, UK) was used to reduce the diameter of polystyrene nanospheres from 500 nm to 250 nm. After that, sputter coating (Quorum Technologies Q150T ES, UK) was performed with 5 nm silver and 10 nm gold on the surface of silicon wafers. Then, ultrasonication for 5 minutes was performed to remove the polystyrene nanospheres. 20 mL of $H_2O$, 1 mL of HF and 0.2 mL of $H_2O_2$ solution were added one by one for chemical etching of the nanopillars. Finally, 2 nm of titanium and 50 nm of gold were sputter coated onto the nanopillars, obtaining complete gold nanopillar chips. Electronic microscopic images of the nanopillars were obtained by scanning electron microscopy (SEM, ZEISS Sigma HD VP FE-SEM, Germany). The reflectance of the as-made nanopillar chips was measured in the integrated sphere of ultraviolet–visible spectroscopy (UV-Vis, Shimadzu UV-2600, UK).

### Sample preparation

**Binding $Ni^{2+}$ to NTA.** 5 mL of 5 mM $NiCl_2$ was added to react with 5 mL of 5 mM NTA ethanol solution for 24 h to form an NTA–Ni structure.

**Hydrophilicity of gold nanopillars.** To clean the gold nanopillars, they were rinsed in ethanol and $H_2O$. Then, an oxygen plasma treatment (Gambetti Tecnologia Colibri bench-top plasma system, Italy) was performed to make them hydrophilic. The parameters of oxygen plasma are 50 mW power, 30 s, three times.

**NTA–Ni coating of gold nanopillars.** 2 mL of NTA–Ni solution was added to a 60 × 15 mm Petri dish; then, gold nanopillar chips were placed in this Petri dish for 24–48 hours, and gold nanopillars with NTA–Ni chips (AuNP–NTA–Ni) were obtained.

**Binding Pro or Hyp to AuNP–NTA–Ni.** Ethanol and $H_2O$ were used to clean the extra NTA–Ni on the surface of AuNP–NTA–Ni chips. 2 mL of 100 nM Pro or 100 nM Hyp neutral solution was added directly to the AuNP–NTA–Ni solution for Raman measurements.

### XPS analysis

X-ray photoelectron spectroscopy (XPS, Thermo Fisher Scientific ESCALAB 250Xi XPS, USA) was used to study the surface binding mechanism.

### Raman measurements

Raman spectroscopy was performed using a Thermo Scientific DXR2xi Raman imaging microscope. The working parameters were a laser wavelength of 785 nm, an exposure time of 0.1–1 s per spectrum, a laser power of 2.5–10 mW, and a 60× water-immersion objective. Finally, Andor Solis software was used to collect the data; it collected 2000 spectra per dataset at the same time. Raman data analysis was performed using MATLAB R2022a and Origin 2022b software.

### Finite-element method (FEM) simulation of gold nanopillars

FEM (COMSOL Multiphysics, COMSOL Co. Ltd) was used for numerical calculations. The optical parameters of gold and silicon were adopted from the literature.[26,27] For accuracy, the finest mesh size was set to no more than 2 nm. Linearly polarized plane waves (the electric field direction is parallel to the *x*-axis) were incident perpendicularly to the structure. Periodic boundary conditions were applied on horizontal borders. The periods along the *x* and *y* axes were set as 500 nm. The length and diameter of the nanopillar were 800 nm and 250 nm, respectively, the gold coating thickness was 50 nm, and the radius of the nanopillar cup was 100 nm.

### Data pre-processing and peak assignment

**Peak assignments.** MATLAB was used to do peak assignments and draw SERS spectral figures. The main steps are: (1) plotting the SERS spectra of 2000 raw data; (2) cosmic ray removal: remove interference from the Raman instrument; (3) normalization: make all spectra have the same baseline; (4) background removal: reduce other purity influences; (5) signal detection: collect all spectra with good signal; (6) finding peaks: use the Pro and Hyp databases to find their peaks in spectra; (7) output figure results.

**Distribution histograms of peak occurring frequency.** MATLAB scripts were used to calculate the peak occurring frequency at each Raman shift. The steps include: (1) pretreatment of multiple data; (2) extracting effective spectra: find all spectra with rich signals; (3) find peak frequency: summarize each peak's occurring frequency in all spectra; (4) output excel results; (5) draw histograms: Origin software was used to draw the distribution histograms of the SERS peaks.

**Event histograms of intensity–time traces.** Clampfit and Origin software were used for *T* bind and *T* release event histograms. The main steps are: (1) import the time trace figure to Clampfit; (2) event detection; (3) single-channel search; (4) set *T* release as 0 and *T* bind as 1; (5) run as nonstop; (6) export all events data in one excel file; (7) use Origin to draw event histograms.

### Deep learning classification

**One-dimensional convolutional neural network (1D-CNN) model.** MATLAB was used to run the codes of the 1D-CNN model for classification and post-evaluation. A total of 6000 and 2000 peak assignment selected spectra with 1463 features were classified using 5-fold cross-validation for the 1D-CNN classification model and post-evaluation model, where 80% of the spectra were used as the training set and 20% of the spectra were used as the test set. The steps are as follows: (1) dataset preparation; (2) training process; (3) evaluation metrics.

## 3. Results and discussion

### Sensor fabrication and measurement

For the experimental process, Fig. 1a shows the *in situ* Raman measurements of Pro and Hyp using gold nanopillars. As conceptualized in Fig. 1b, NTA was covalently attached to the surface of gold nanopillars by thiol bonding, and then reacted with $Ni^{2+}$ to form NTA–Ni as the specific affinity agent to capture Pro and Hyp as NTA–Ni–Pro and NTA–Ni–Hyp through chelation. The gold nanopillar has the advantage of having a stable wide-range hot spot (Fig. 1c) with a decay length of around 50 nm for reproducible SERS detection of large and long molecule moieties.[19,20] As the length of NTA–Ni–Pro (NTA–Ni–Hyp) is short,[28] the hot spot of the gold nanopillars can cover all chains of the molecules to provide convoluted SERS spectra of both NTA–Ni and Pro (Hyp). The finite element method (FEM) simulation of the AuNPs with a diameter of 250 nm shows a wide-range hot spot at 785 nm wavelength (Fig. 1c) when the simulated reflectance shows a localized surface plasmon resonance (LSPR) at 790 nm (Fig. S1a). Accordingly, we fabricated AuNPs of similar diameter, with a height of around 1 μm and a period of around 500 nm (Fig. 1d). The measured reflectance shows that its LSPR dip is at 786 nm (Fig. S1b). The fabricated AuNPs have a uniform surface and a stable structure (Fig. S2). These results demonstrate that the fabricated AuNPs can provide reproducible SERS spectra with a wide-range hot spot.

To test the binding capability of NTA to capture Pro or Hyp, we conducted *in situ* Raman measurement to collect 2000 time-series SERS spectra with 0.1 s exposure time of molecules in different systems: AuNP–NTA–Ni–Pro (Fig. 1e), AuNPs (Fig. S3a), and AuNP–Pro (Fig. S3b). NTA–Ni was incubated on the AuNPs for 24–48 hours to form the AuNP–NTA–Ni structure as confirmed by the XPS analysis in Fig. S4. As a control sample of bare AuNPs, no SERS signals were observed on AuNPs themselves (Fig. S3a). When the Pro solution was directly added to the Petri dish containing the bare AuNP chips, the water-immersion objective was dipped into it immediately for SERS measurement. Such diffusion of Pro near the AuNPs for a short time also did not show any SERS signals (Fig. S3b). In the case of using AuNP–NTA–Ni to bind Pro molecules, the SERS time-series spectra in Fig. 1e show that the unique Raman bands at 411 $cm^{-1}$ and 618 $cm^{-1}$ are from aromatic ring bending, 1225 $cm^{-1}$ corresponds to the Pro ring deformation of $CH_2$ and $NH_2$, and 825 $cm^{-1}$ attributed to ring stretching, demonstrating the successful binding of Pro.[15,16] The 618 $cm^{-1}$ shifts to 648 $cm^{-1}$ due to the changes of the Pro conformation. Fig. 1f shows the representative stochastic SERS time traces of the Pro band at 825 $cm^{-1}$, in which the pulses were from the binding of AuNP–NTA–Ni to the Pro molecules and the baseline reflected the release of Pro from AuNP–NTA–Ni. Other peak assignments' information can be found in Table S2. Moreover, we observed fluctuation of the SERS band position of AuNP–NTA–Ni–Pro, such as the 825 and 1225 $cm^{-1}$ bands in Fig. 2a and those in Fig. S5, which could be due to the conformation changes of AuNP–NTA–Ni–Pro.[15]

### Peak frequency analysis

Similarly, we observed stochastic and fluctuating SERS spectra of AuNP–NTA–Ni–Hyp as shown in Fig. 2c and Fig. S6. The band fluctuation is challenging for traditional analysis by SERS band intensities, because averaging band by intensity would broaden the SERS peak and decrease the spectral resolution. To study the SERS band difference between AuNP–NTA–Ni–Pro and AuNPs–NTA–Ni–Hyp, we used a statistical method to draw distribution histograms of the occurrence frequency for peak assignments.[29] It can extract specific features from fluctuated SERS spectra and reduce the influence of the peak intensity, demonstrating a high spectral resolution that the traditional SERS analysis cannot provide. The histograms of the occurrence frequency for all SERS spectra of AuNP–NTA–Ni–Pro and AuNP–NTA–Ni–Hyp are summarized in Fig. 2b and

 

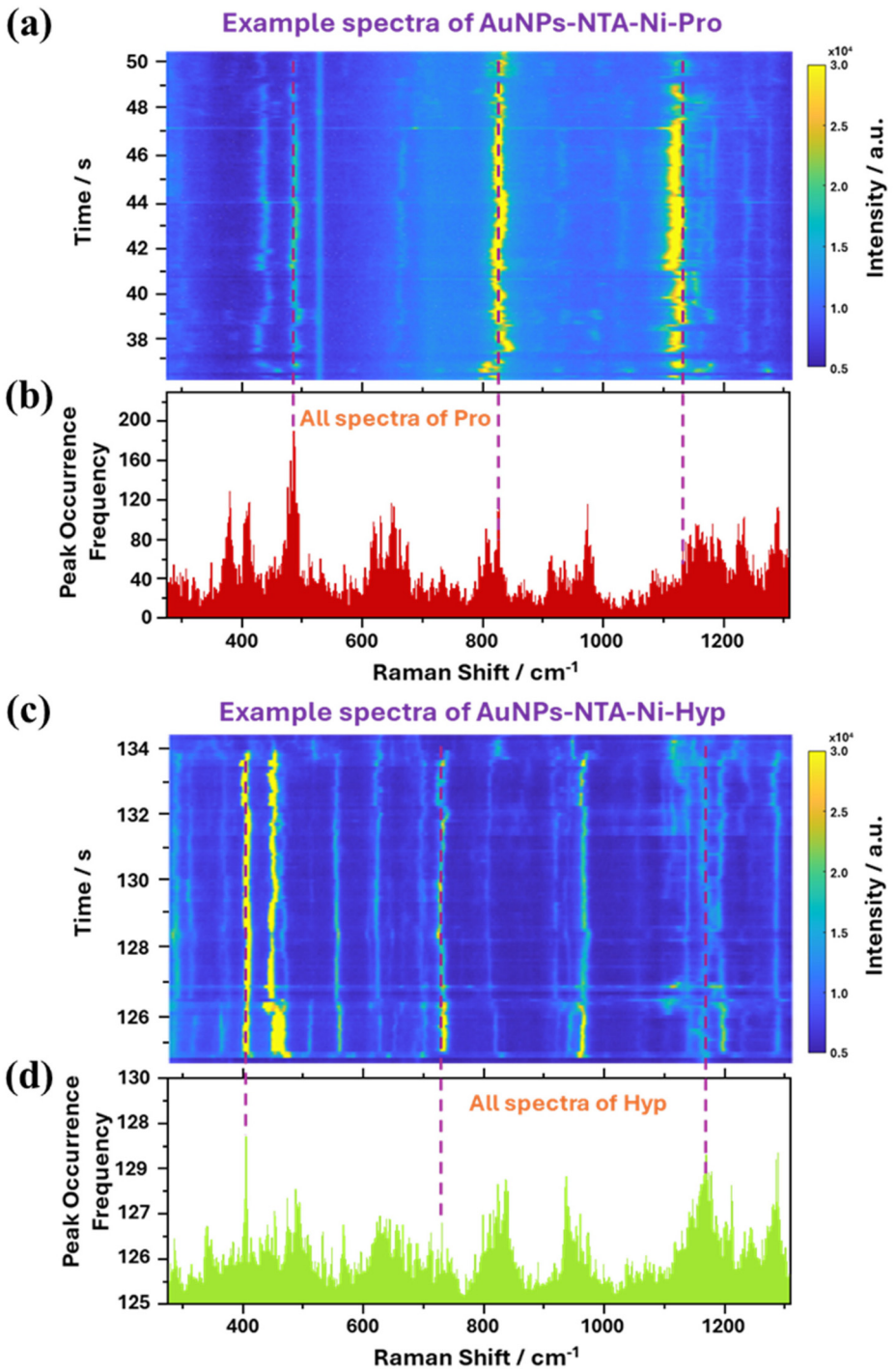


**Fig. 2** SERS time-series spectra of AuNP–NTA–Ni–Pro (a) and AuNP–NTA–Ni–Hyp (c). Distribution histograms and peak assignments of the occurrence frequency for AuNP–NTA–Ni–Pro (b) and AuNP–NTA–Ni–Hyp (d) at each peak position.

d, respectively, where the peak assignment information can be found in Table S2.

Fig. 2b shows the longest column bar at 485 $cm^{-1}$ due to the Pro ring vibration, and the nearest peak at 455 $cm^{-1}$ is also from the same vibration mode in AuNP–NTA–Ni–Pro. Other Pro ring bending bands[16] at 349, 380, 411, and 618 $cm^{-1}$ show an obvious fluctuation at 380 $cm^{-1}$ from 362 to 392 $cm^{-1}$, probably due to molecular fluctuations when NTA–Ni captures Pro. There is a subtle wavenumber shift from 1233 $cm^{-1}$ to 1247 $cm^{-1}$ due to deformation with $CH_2$ and $NH_2$.[15] These aromatic ring modes indicate that Pro molecules entered the hot spot of AuNPs to obtain enhanced signals. Another higher column at 1290 $cm^{-1}$ was assigned to bending of the CH and NH groups;[16] these are part of the Pro ring moiety.

Particularly, the band of nickel with oxygen[16] was obtained at 286 $cm^{-1}$; it demonstrated that nickel was attached to AuNP–NTA.

Under the same conditions, Fig. 2d shows Hyp information in the AuNP–NTA–Ni–Hyp system, with the longest column at 405 $cm^{-1}$ due to Hyp ring bending. Hyp has many vibration modes that are common with Pro due to their similar molecular structure. The strong band shifting from 1210 to 1245 $cm^{-1}$ belongs to Hyp ring deformation with $CH_2$ and $NH_2$,[15] respectively. The higher column at 1288 $cm^{-1}$ shows bending of CH and NH from the ring. It is reasonable to assume a configuration of AuNP–NTA–Ni–Hyp in which Hyp bending itself occurs close to the gold nanopillar;[30] Hyp has an exceptional amino acid ring with tryptophan, so they have a similar mechanism of interaction between the molecule and the gold substrate in SERS measurement. There is one band at 285 $cm^{-1}$ associated with nickel ions and oxygen binding as Pro. Particularly, Hyp has a strong band at 1169 $cm^{-1}$, which is assigned to NH bending.[15,16] Fig. 2b and d show the overall change trend of the Pro/Hyp molecules in the AuNP–NTA–Ni–Pro/Hyp system. The characteristic peak information analyzed above proves that the AuNP–NTA–Ni system has high sensitivity in detecting Pro and Hyp.

### Stochastic quantification of Pro and Hyp

To quantify Pro and Hyp by this method, pure Pro and Hyp at varying concentrations were first measured to establish linear relationships between characteristic peak frequencies and concentrations. To calculate the limit of detection (LoD) of this method, we detected pure Pro and Hyp solutions of different concentrations to obtain the linear relationship between two characteristic peak frequencies of Pro/Hyp and concentration (Fig. S5 and S6). Firstly, we used a series of concentrations of Pro and Hyp solution of 1 fM, 10 fM, 100 fM, 1 pM, 10 pM, 100 pM, 1 nM, 10 nM, 100 nM, and 1 μM. After obtaining their corresponding time series Raman spectra, we generated distribution histograms of peak frequencies. Then, we used the ratio of two characteristic peak frequencies of Pro (825, 935 $cm^{-1}$ for ring stretching[15,16]) to the silicon frequency (520 $cm^{-1}$) to the concentration to obtain a good linear relationship diagram in Fig. 3a and b with $R^2$ = 0.998 and 0.996, respectively. We fabricated gold nanopillars by coating a gold layer on silicon nanopillars, so there is one silicon peak at 520 $cm^{-1}$. The intensity of the silicon peak was affected by (1) nanopillar uniformity, as the nanopillars coated with a thin gold layer exhibited high silicon peak intensity and *vice versa*; and (2) intensities of SERS signals from the Pro/Hyp bond because large amounts of Pro/Hyp bond would generate strong SERS signals and baseline to overlap the silicon peak. By choosing the silicon peak as the internal standard, these issues of sample uniformity and bond analyte amount were all corrected.

Similarly, Hyp peaks at 405 $cm^{-1}$ (ring bending) and 1247 $cm^{-1}$ (ring stretching)[15,16] also exhibited strong linear correlations with concentration with $R^2$ = 0.986 and 0.981 as shown in Fig. 3c and d, respectively. The calculated LoDs for Pro were 0.189 pM for the 825 $cm^{-1}$ band and 0.212 pM for the 935 $cm^{-1}$ band, while those for Hyp were 0.434 pM for the 405 $cm^{-1}$ band and 0.576 pM for the 1247 $cm^{-1}$ band. These results show that AuNP–NTA–Ni can obtain Pro and Hyp signals in the pM range, which has high sensitivity in the quantification of biomolecules.

To demonstrate our method for quantification of Pro and Hyp in the mixture, we tested it using mixtures of five amino acids (Pro, Hyp, Cys, His, Ser)[31–33] across six concentrations from 10 pM to 1 μM (Table 1). Following the same measurement procedure, frequencies of the characteristic peaks of Pro (825 and 935 $cm^{-1}$) and Hyp (405 and 1247 $cm^{-1}$) were normalized to those of the silicon peak at 520 $cm^{-1}$. The lowest concentration of Pro and Hyp in the mixture was chosen when the normalized frequencies ranged from 0.8 to 1. As shown in Fig. 4, both exhibited excellent linear responses with $R^2$ = 0.992 and 0.991 for Pro and 0.988 and 0.996 for Hyp with LoDs of 0.184 nM, 0.209 nM, 0.329 nM, and 0.137 nM, respectively. These findings highlight the potential of AuNP–NTA–Ni not only for amino acid mixtures, but also for detecting hydroxylated biomolecules such as HIF-1α proteins.[34–36]

### Stochastic binding kinetics

The LoDs of Pro and Hyp in the mixture are almost 3 orders lower than those in pure solution, which highlighted the competitive chelation binding of the AuNP–NTA–Ni to the Pro/Hyp by other amino acids in the mixture. To study the competitive binding, we calculated the time constants of association ($k_{on}$) and dissociation ($k_{off}$) with SERS time traces with intensity changes.[22] As shown in Fig. 5a and b, the time traces of the Raman intensity of the SERS peak at 825 $cm^{-1}$ for Pro and 405 $cm^{-1}$ for Hyp were extracted from the corresponding SERS time series of specific concentrations in Fig. S5 and S6. The duration of the transient binding event corresponds to high Raman intensity with the binding time ($T$-bind), *i.e.* the time the Pro/Hyp remains bound to the AuNP–NTA–Ni. Conversely, the duration of the low-Raman-intensity event represents the interval between two consecutive binding events ($T$-release). Similar traces were also observed for pure Hyp and Pro in different concentrations (Fig. S7 and S8).

Fig. 5c and d show the examples of the extracted histogram distributions of the $T$-bind and $T$-release which are well described by single-exponential statistics to $\exp(t/T)$, where $T$ is the characteristic time constant, indicating stochastic first-order association/dissociation dynamics at the dominant hotspot receptor. Histograms of different concentrations are shown in Fig. S9 and S10. The reciprocal of the characteristic binding time $1/\langle T_{bind}\rangle$ increases linearly with analyte concentration [P]: $1/\langle T_{bind}\rangle = k_{on}[P]$ as shown in Fig. 5e, yielding the association rate constant $k_{on}$. Then, the dissociation frequency $1/\langle T_{release}\rangle$ is essentially concentration-independent (Fig. 5f), yielding the dissociation rate constant $k_{off} = 1/\langle T_{release}\rangle$. From the slopes and plateaus, we extracted $k_{on,\ pure\ Pro} = (4.20 \pm 0.5) \times 10^4\ M^{-1}\ s^{-1}$ and $k_{on,\ pure\ Hyp} = (4.63 \pm 0.5) \times 10^4\ M^{-1}\ s^{-1}$, while $k_{off,\ pure\ Pro} = 0.22 \pm 0.05\ s^{-1}$ and $k_{off,\ pure\ Hyp} = 0.26 \pm 0.07\ s^{-1}$. Similarly, in Fig. 5g and h, the Pro and Hyp in mixture

 

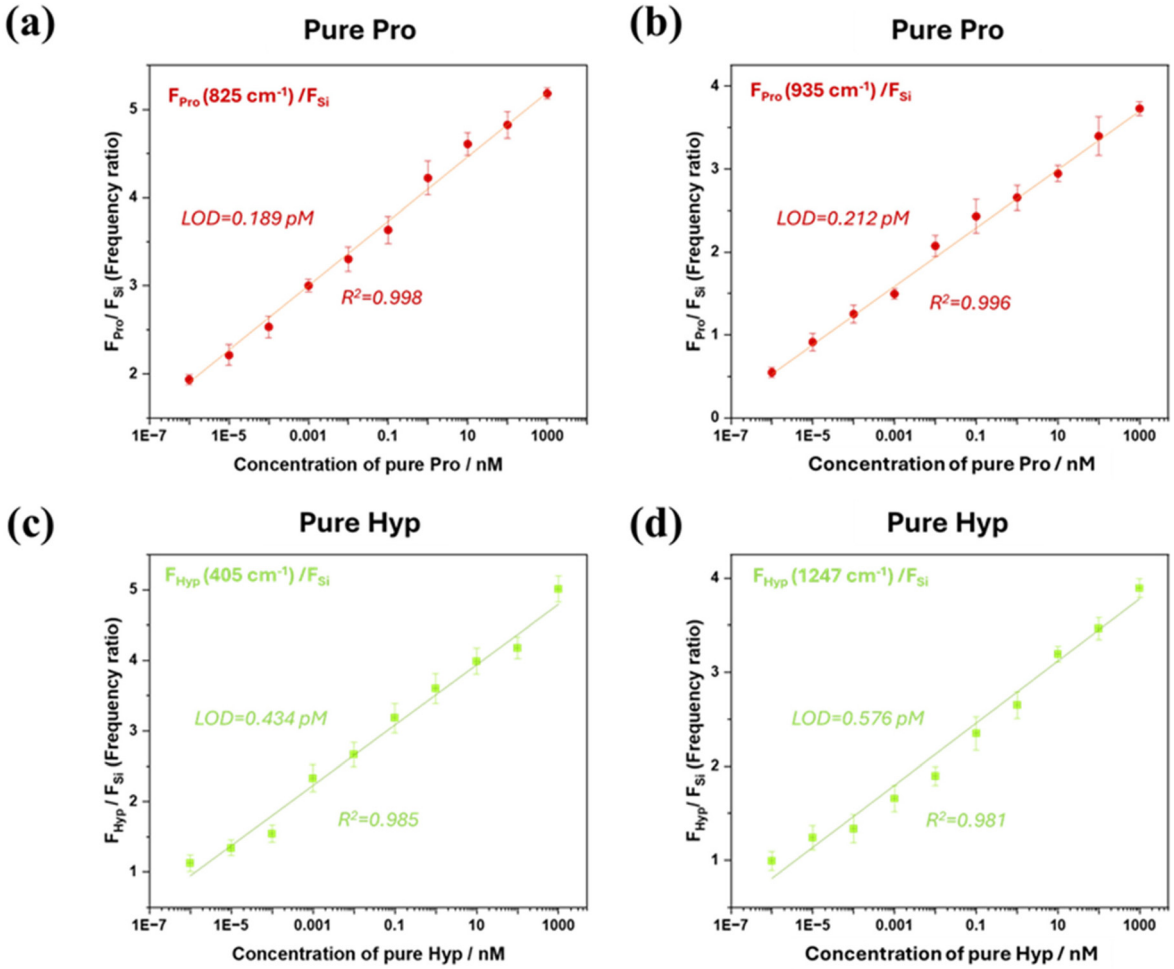


**Fig. 3** Stochastic quantification of pure Pro and Hyp. The linear fit of Pro and Hyp Raman peak frequency ratio of Pro at 825 $cm^{-1}$ (a) and 935 $cm^{-1}$ (b) and Hyp at 405 $cm^{-1}$ (c) and 1257 $cm^{-1}$ (d) at 1 fM to 1 μM pure Pro and Hyp concentrations. The error bars indicate the standard deviations of the peak frequency ratio for all the spectra over the detected area. Linear regression of the concentrations indicated excellent concordance between the actual and predicted results, with $R^2$ values of 0.998, 0.996, 0.985, and 0.981 for Pro (a and b) and Hyp (c and d), respectively.

**Table 1** The concentrations of Pro, Hyp and other amino acids in the mixture

| Mixture no. | Pro | Hyp | Cys | His | Ser |
|---|---|---|---|---|---|
| 1 | 10 pM | 10 pM | 10 pM | 10 pM | 10 pM |
| 2 | 100 pM | 100 pM | 100 pM | 100 pM | 100 pM |
| 3 | 1 nM | 1 nM | 1 nM | 1 nM | 1 nM |
| 4 | 10 nM | 10 nM | 10 nM | 10 nM | 10 nM |
| 5 | 100 nM | 100 nM | 100 nM | 100 nM | 100 nM |
| 6 | 1 μM | 1 μM | 1 μM | 1 μM | 1 μM |

demonstrated concentration-dependent $k_{on,\ mix\ Pro}$ = (7.60 ± 0.9) $M^{-1}$ $s^{-1}$ and $k_{on,\ mix\ Hyp}$ = (7.08 ± 0.8) $M^{-1}$ $s^{-1}$ and the concentration-independent $k_{off,\ mix\ Pro}$ = 0.25 ± 0.06 $s^{-1}$ and $k_{off,\ mix\ Hyp}$ = 0.24 ± 0.08 $s^{-1}$.

These results confirm the reversible bimolecular interaction between the amino acids and the NTA receptor on the gold nanopillar with similar probabilities: *e.g.* NTA–Ni + Hyp ⇌ NTA–Ni·Hyp in both pure solution and mixture. It is reasonable to assume that the binding kinetics of Pro and Hyp were similar due to the tiny difference in their molecular structures by the small hydroxyl group. Meanwhile, the competing binding from other amino acids decreased the association rate constants of Pro and Hyp in mixture ($k_{on,\ mix\ Hyp}$ and $k_{on,\ mix\ Pro}$) by almost 4 orders against those in pure solution ($k_{on,\ pure\ Hyp}$ and $k_{on,\ pure\ Pro}$). This contributed to the 3-order difference between the LoDs of the AnNP–NTA–Ni sensors in pure solution and mixture.

Moreover, the higher $k_{on,\ mix\ Pro}$ = (7.60 ± 0.9) $M^{-1}$ $s^{-1}$ than the $k_{on,\ mix\ Hyp}$ = (7.08 ± 0.8) $M^{-1}$ $s^{-1}$ meant higher binding probability of Pro than that of Hyp to the AuNP–NTA–Ni in the mixture. This led to lower average LoD of Pro in mixture as 0.20 nM by the 825 and 935 $cm^{-1}$ peaks (Fig. 4a and b) than that of Hyp in mixture as 0.23 nM from the 405 and 1247 $cm^{-1}$ peaks (Fig. 4c and d). However, the LoD of Hyp in mixture (0.137 nM) calculated from the 1247 $cm^{-1}$ peaks did not follow this trend, which might be due to the Hyp conformation change and resultant fluctuating SERS bands. This suggests

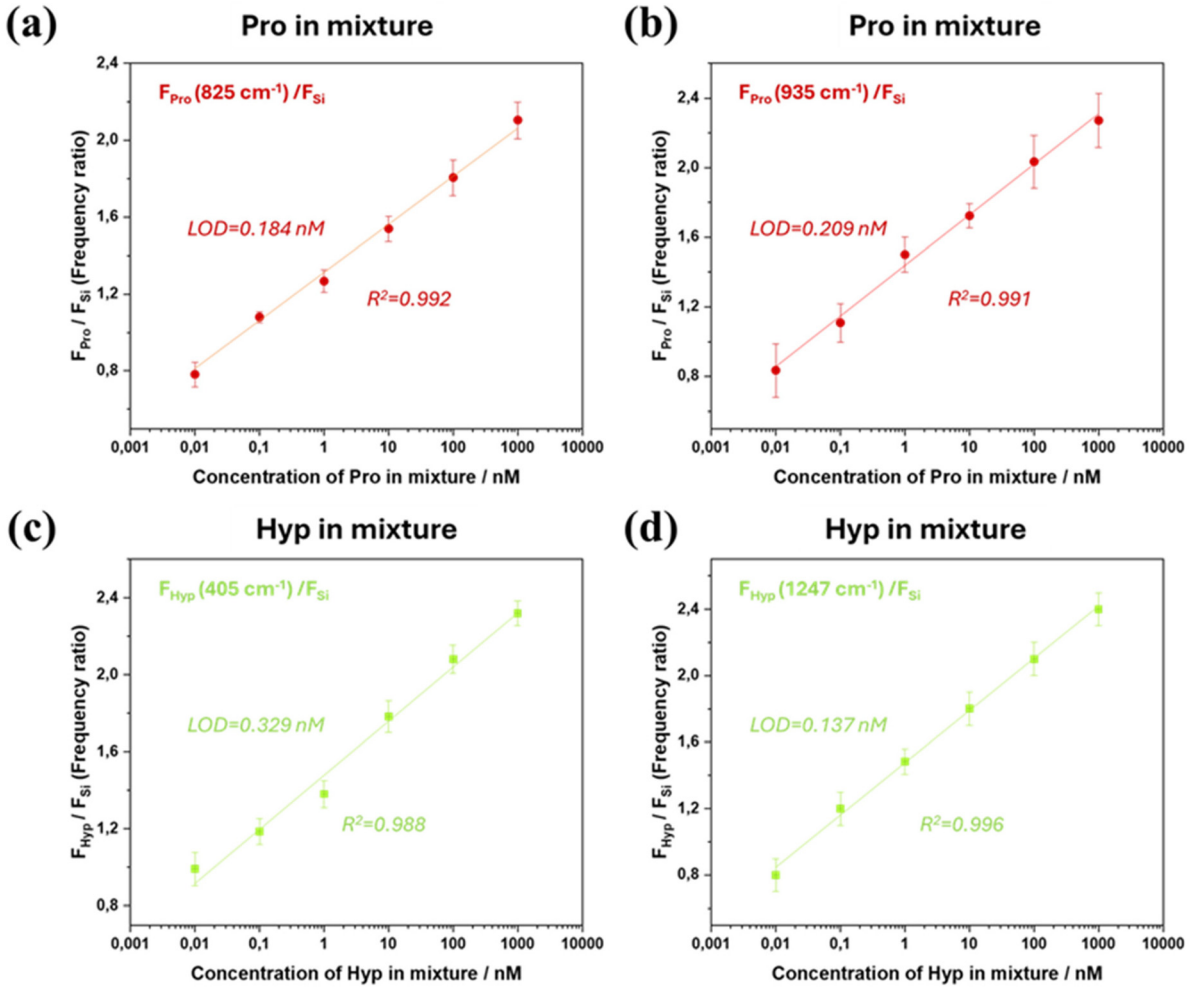


**Fig. 4** Stochastic quantification of Pro and Hyp in mixture. The linear fit of Pro and Hyp Raman peak frequency ratio of Pro at 825 $cm^{-1}$ (a) and 935 $cm^{-1}$ (b) and Hyp at 405 $cm^{-1}$ (c) and 1257 $cm^{-1}$ (d) at 10 pM to 1 μM pure Pro and Hyp concentrations. The error bars indicate the standard deviations of the peak frequency ratio for all the spectra over the detected area. Linear regression of the concentrations indicated excellent concordance between the actual and predicted results, with $R^2$ values of 0.992, 0.991, 0.988, and 0.996 for Pro (a and b) and Hyp (c and d), respectively.

that the SERS band fluctuation affected the LoD significantly and the LoD calculation using a single SERS band is not reliable.

### Deep learning identification

The SERS band fluctuation of AuNP–NTA–Ni–Pro and AuNP–NTA–Ni–Hyp necessitated the use of deep learning models for data analysis and identification. Accordingly, we developed a one-dimensional convolutional neural network (1D-CNN) model for the spectral classification of AuNP–NTA–Ni–Pro and AuNP–NTA–Ni–Hyp as shown in Fig. 6a. 6000 spectra of AuNP–NTA–Ni–Pro and AuNP–NTA–Ni–Hyp, respectively, were divided as 4800 spectra for model training and 1200 ones for testing. Fig. S11a shows the low loss curve and the high accuracy curve of the training model with increasing training epochs, which indicates the great classification performance of the trained 1D-CNN model for identifying the AuNP–NTA–Ni–Pro and AuNP–NTA–Ni–Hyp spectra. For the training set of 4800 spectra data of AuNP–NTA–Ni–Pro and AuNP–NTA–Ni–Hyp, the classification accuracies are 99.5% for Pro and 99.1% for Hyp, as presented in Fig. S11b. While at the testing step of 1200 spectra, the classification accuracies for the Pro and Hyp were 96.5% for Hyp and 95.9% for Pro in Fig. 6b.

The CNN operates on individual single-shot spectra, each of which corresponds to one time point within the 2000-frame SERS time series (0.1 s per frame). Spectra are not averaged, not grouped by time, and no time index is provided to the model. Low-signal spectra are removed through preprocessing and peak assignment, and all remaining spectra are treated as independent samples for classification. To test the practical use of the trained 1D-CNN model, another set of 2000 completely new and independently prepared spectra—acquired on fresh Au nanopillar substrates, on a different measurement day, and using newly prepared NTA–Ni and Pro/Hyp solutions—were fed into the network in a predict-only mode for external post-evaluation analysis. As shown in Fig. 6c, classification

 

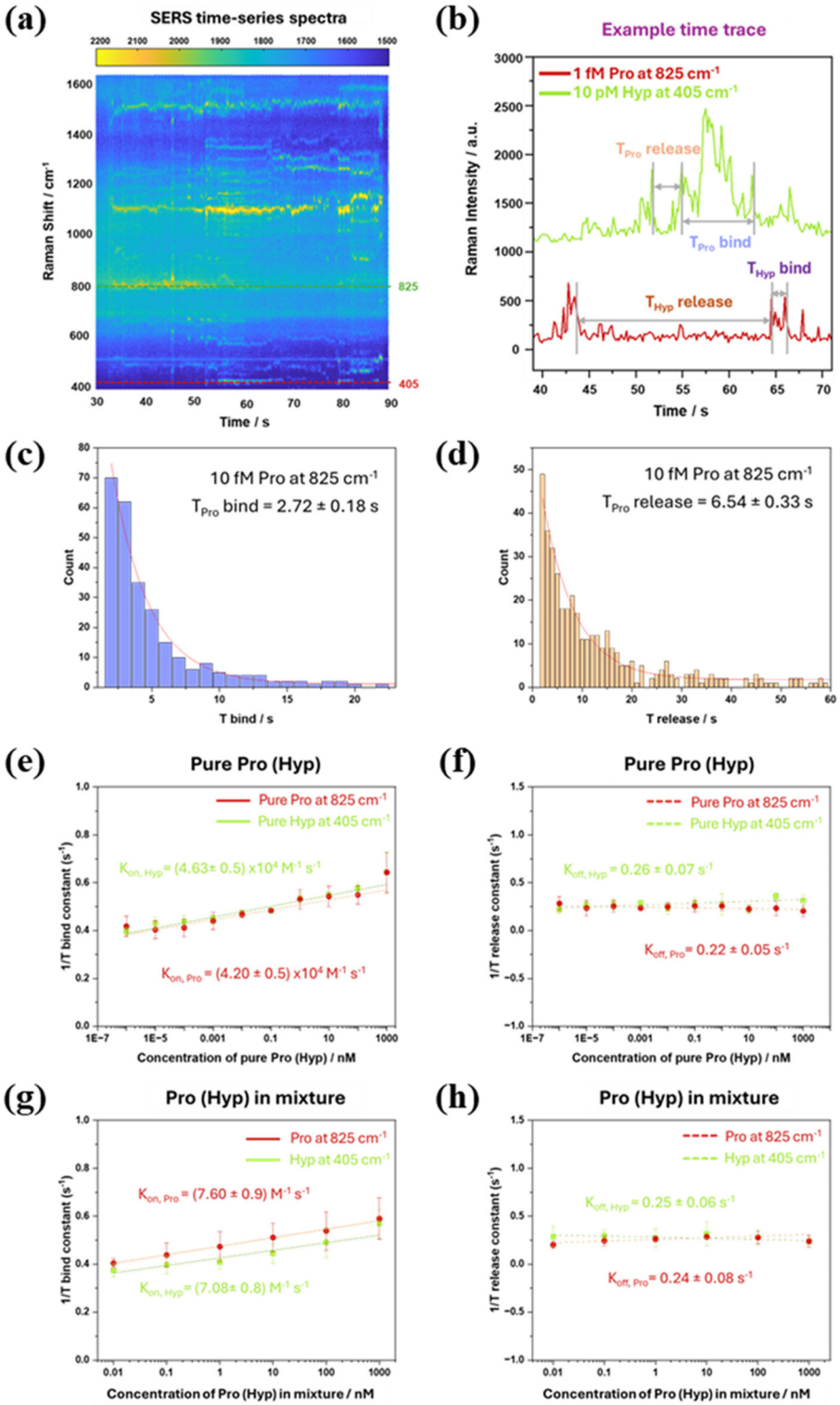


**Fig. 5** Binding kinetics of Pro, Hyp and mixture on NTA-modified gold nanopillars. (a) SERS time-series spectra of Pro/Hyp in mixture. (b) Representative Raman time traces of Pro and Hyp show transient binding and releasing events. (c and d) Event histogram examples of intensity–time traces. *T*_bind represents the binding duration, while *T*_release is the interval between two consecutive binding events. Solid lines indicate single-exponential fits, providing the characteristic time constants *T*-bind and *T*-release. (e–h) Association frequency ($1/\langle T_{bind}\rangle$) and dissociation frequency ($1/\langle T_{release}\rangle$) as functions of Pro, Hyp (e and f) and mixture (g and h) at their varying concentrations. The solid lines show linear fits used to extract the association rate, whereas the dotted lines represent constant fits used to determine the dissociation rate.

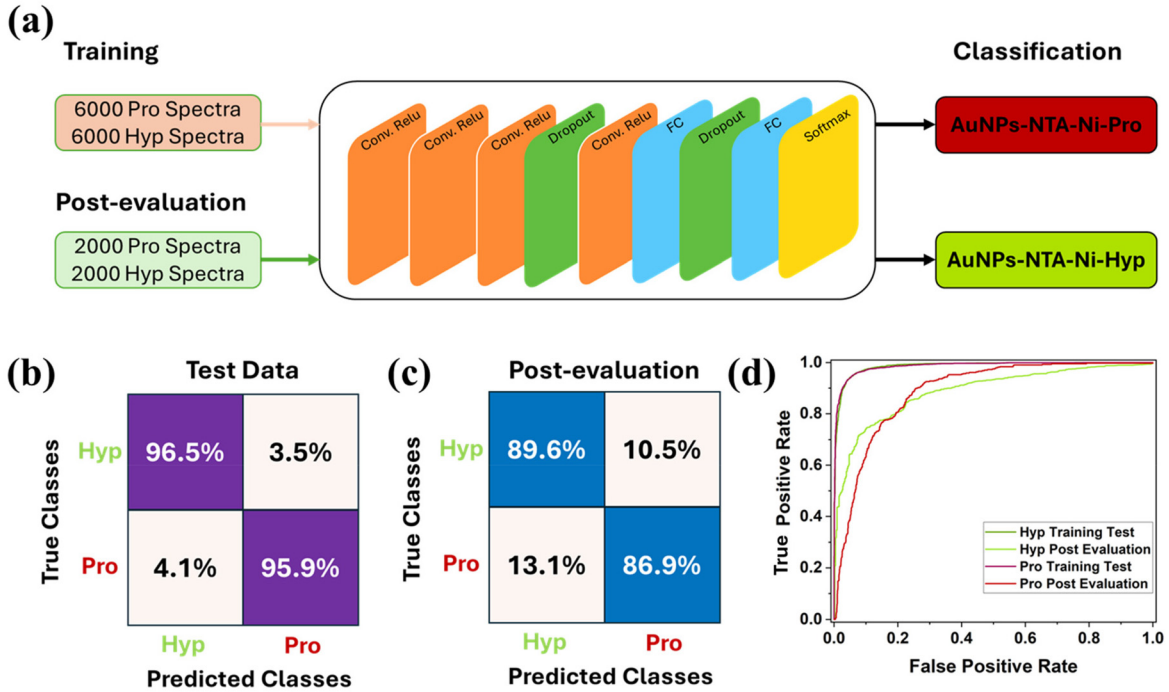


**Fig. 6** Deep learning process for identification of AuNPs–NTA–Ni–Pro and AuNPs–NTA–Ni–Hyp by a 1D-CNN model. (a) The architecture of the 1D-CNN model. (b) The testing classification accuracy of 96.5% for Hyp and 95.9% for Pro. (c) The post-evaluation classification accuracy of 89.6% for Hyp and 86.9% for Pro. (d) The ROC figure of Hyp and Pro.

accuracy of 89.6% for Hyp and 86.9% for Pro is obtained in the confusion matrix of post-evaluation analysis, demonstrating the significant performance of the trained 1D-CNN model to differentiate new SERS spectra of AuNP–NTA–Ni–Pro and AuNP–NTA–Ni–Hyp. The receiver operating characteristics (ROC) curves are shown in Fig. 6d. It shows both high sensitivity and high specificity of the model in identifying new spectra of Pro and Hyp.

## 4. Conclusion

In summary, the stochastic sensing platform based on AuNP–NTA–Ni was designed and used to reversibly capture and detect Pro and Hyp by SERS. The distribution histograms of occurrence frequency provided the band features between Pro and Hyp, which can be used to achieve fast quantitative analysis within 30 min. Accordingly, we got good LoDs in the mixture as between 0.184 nM and 0.209 nM for Pro and between 0.137 nM and 0.329 nM for Hyp. The transient signals of different bands extracted from the time-series SERS spectra were analyzed for the binding kinetics of AuNP–NTA–Ni to Pro/Hyp. The competitive binding in the mixture from other amino acids decreased the association rate constants of Pro and Hyp by almost 4 orders against those in pure solution, which contributed to the 3-order difference between the LoDs of the AnNP–NTA–Ni sensors in pure solution and mixture. To overcome the uncertainty of LoD calculation by the fluctuating SERS bands, we used the deep learning identification using a 1D-CNN model: the test results of Pro and Hyp are 95.9% and 96.5%, and the post-evaluation results of new data are 86.9% and 89.9%, respectively. Our work demonstrated a new SERS sensing method based on reversible binding and deep learning analysis, setting a base for the challenging hydroxylation detection in, for example, rapid diagnosis for biomarkers of cancer diseases.

## Author contributions

Yuan Zhang fabricated the gold nanopillar chips, determined the Raman measurement protocol, collected Raman spectra, analyzed the Raman spectra, and wrote the manuscript. Kuo Zhan wrote the scripts for Raman data preprocessing and peak occurrence frequency calculation and developed a 1D-CNN model for Pro/Hyp discrimination. Peilin Xin contributed to writing the Raman spectra preprocessing, data selection scripts and revised the manuscript. Yingqi Zhao contributed to the Raman measurement suggestion and revised the manuscript. Ibrar Alam helped draw time trace histograms and revised the manuscript. Shubo Wang provided UV-Vis measurement devices and revised the manuscript. Kai Liu did the simulation and revised the manuscript. Aliaksandr Hubarevich contributed to the gold nanopillar simulation. Xuejin Zhang supervised the simulation. Jianan Huang conceived the idea, acquired funding, supervised the work, and revised the manuscript. The manuscript was written with con-

tributions from all authors. All authors have approved the final version of the manuscript.

## Conflicts of interest

There are no conflicts to declare.

## Data availability

The authors declare that the data supporting the findings of this study are available within this paper and its supplementary information (SI). Data are also available from the corresponding author upon reasonable request.

Supplementary information is available. The supplementary information includes characterization figures, Raman time-series spectra, time-trace spectra, T histograms, and Raman bands assignments table. See DOI: https://doi.org/10.1039/d5nr04125b.

The codes for data analysis and all raw SERS data are available on GitHub. The website link: KuoZHAN/surface-enhanced-Raman-spectroscopic-detection-of-proline-and-hydroxylated-proline-: CNN and post-evaluation model with raw data (https://github.com/KuoZHAN/Surface-enhanced-Raman-spectroscopic-detection-of-proline-and-hydroxylated-proline-).

## Acknowledgements

This research received support from the Biocenter Oulu Emerging Project (DigiRaman), spearhead project 2024–2027 and the DigiHealth project (No. 326291), a strategic profiling project at the University of Oulu that is supported by the Academy of Finland and the University of Oulu. Yuan Zhang acknowledges the China Scholarship Council for a scholarship for doctoral study at the University of Oulu. The authors thank Professor Xia Yang (Southwest University, China) for valuable discussion about NTA binding.

## References

1 L. Szabados and A. Savouré, Proline: A Multifunctional Amino Acid, *Trends Plant Sci.*, 2010, **15**(2), 89–97, DOI: 10.1016/j.tplants.2009.11.009.

2 G. L. Semenza, Regulation of Mammalian O $_2$ Homeostasis by Hypoxia-Inducible Factor 1, *Annu. Rev. Cell Dev. Biol.*, 1999, **15**(1), 551–578, DOI: 10.1146/annurev.cellbio.15.1.551.

3 P. H. Maxwell, M. S. Wiesener, G.-W. Chang, S. C. Clifford, E. C. Vaux, M. E. Cockman, C. C. Wykoff, C. W. Pugh, E. R. Maher and P. J. Ratcliffe, The Tumour Suppressor Protein VHL Targets Hypoxia-Inducible Factors for Oxygen-Dependent Proteolysis, *Nature*, 1999, **399**(6733), 271–275, DOI: 10.1038/20459.

4 R. K. Bruick and S. L. McKnight, A Conserved Family of Prolyl-4-Hydroxylases That Modify HIF, *Science*, 2001, **294**(5545), 1337–1340, DOI: 10.1126/science.1066373.

5 A. C. R. Epstein, J. M. Gleadle, L. A. McNeill, K. S. Hewitson, J. O'Rourke, D. R. Mole, M. Mukherji, E. Metzen, M. I. Wilson, A. Dhanda, Y.-M. Tian, N. Masson, D. L. Hamilton, P. Jaakkola, R. Barstead, J. Hodgkin, P. H. Maxwell, C. W. Pugh, C. J. Schofield and P. J. C. Ratcliffe, Elegans EGL-9 and Mammalian Homologs Define a Family of Dioxygenases That Regulate HIF by Prolyl Hydroxylation, *Cell*, 2001, **107**(1), 43–54, DOI: 10.1016/S0092-8674(01)00507-4.

6 M. Ivan, K. Kondo, H. Yang, W. Kim, J. Valiando, M. Ohh, A. Salic, J. M. Asara, W. S. Lane and W. G. Kaelin Jr, HIFα Targeted for VHL-Mediated Destruction by Proline Hydroxylation: Implications for O $_2$ Sensing, *Science*, 2001, **292**(5516), 464–468, DOI: 10.1126/science.1059817.

7 P. Jaakkola, D. R. Mole, Y.-M. Tian, M. I. Wilson, J. Gielbert, S. J. Gaskell, A. von Kriegsheim, H. F. Hebestreit, M. Mukherji, C. J. Schofield, P. H. Maxwell, C. W. Pugh and P. J. Ratcliffe, Targeting of HIF-α to the von Hippel-Lindau Ubiquitylation Complex by O $_2$ -Regulated Prolyl Hydroxylation, *Science*, 2001, **292**(5516), 468–472, DOI: 10.1126/science.1059796.

8 T. Zhou, L. Erber, B. Liu, Y. Gao, H.-B. Ruan and Y. Chen, Proteomic Analysis Reveals Diverse Proline Hydroxylation-Mediated Oxygen-Sensing Cellular Pathways in Cancer Cells, *Oncotarget*, 2016, **7**(48), 79154–79169, DOI: 10.18632/oncotarget.12632.

9 R. J. McAnulty, *Methods for Measuring Hydroxyproline and Estimating In Vivo Rates of Collagen Synthesis and Degradation, in Fibrosis Research*, Humana Press, Totowa, NJ, 2005, pp. 189–207. DOI: 10.1385/1-59259-940-0:189.

10 A. K. Srivastava, P. Khare, H. K. Nagar, N. Raghuwanshi and R. Srivastava, Hydroxyproline: A Potential Biochemical Marker and Its Role in the Pathogenesis of Different Diseases, *Curr. Protein Pept. Sci.*, 2016, **17**(6), 596–602, DOI: 10.2174/1389203717666151201192247.

11 E. Ábrahám, C. Hourton-Cabassa, L. Erdei and L. Szabados, Methods for Determination of Proline in Plants, *Methods Mol. Biol.*, 2010, **639**, 317–331, DOI: 10.1007/978-1-60761-702-0_20.

12 T. Shen, C. Zhang, F. Liu, W. Wang, Y. Lu, R. Chen and Y. He, High-Throughput Screening of Free Proline Content in Rice Leaf under Cadmium Stress Using Hyperspectral Imaging with Chemometrics, *Sensors*, 2020, **20**(11), 3229, DOI: 10.3390/s20113229.

13 J. F. Cotte, H. Casabianca, B. Giroud, M. Albert, J. Lheritier and M. F. Grenier-Loustalot, Characterization of Honey Amino Acid Profiles Using High-Pressure Liquid Chromatography to Control Authenticity, *Anal. Bioanal. Chem.*, 2004, **378**(5), 1342–1350, DOI: 10.1007/s00216-003-2430-z.

14 S. W. P. Chan, J. Greaves, N. A. Da Silva and S.-W. Wang, Assaying Proline Hydroxylation in Recombinant Collagen Variants by Liquid Chromatography-Mass Spectrometry,

*BMC Biotechnol.*, 2012, **12**(1), 51, DOI: 10.1186/1472-6750-12-51.

15 J. J. Cárcamo, A. E. Aliaga, E. Clavijo, C. Garrido, J. S. Gómez-Jeria and M. M. Campos-Vallette, Proline and Hydroxyproline Deposited on Silver Nanoparticles. A Raman, SERS and Theoretical Study, *J. Raman Spectrosc.*, 2012, **43**(6), 750–755, DOI: 10.1002/jrs.3092.

16 A. R. Guerrero and R. F. Aroca, Surface–enhanced Raman Scattering of Hydroxyproline, *J. Raman Spectrosc.*, 2012, **43**(4), 478–481, DOI: 10.1002/jrs.3065.

17 Y. Zhao, K. Zhan, P.-L. Xin, Z. Chen, S. Li, F. De Angelis and J.-A. Huang, Single-Molecule SERS Discrimination of Proline from Hydroxyproline Assisted by a Deep Learning Model, *Nano Lett.*, 2025, **25**(18), 7499–7506, DOI: 10.1021/acs.nanolett.5c01177.

18 Z. Yang, G. Chen, J. Shen, C. Ma, J. Gu, C. Zhu, L. Li and H. Gao, A Hydrogen Bonding Based SERS Method for Direct Label-Free L-Hydroxyproline Detection, *Spectrochim. Acta, Part A*, 2023, **299**, 122834, DOI: 10.1016/j.saa.2023.122834.

19 J.-A. Huang, Y.-Q. Zhao, X.-J. Zhang, L.-F. He, T.-L. Wong, Y.-S. Chui, W.-J. Zhang and S.-T. Lee, Ordered Ag/Si Nanowires Array: Wide-Range Surface-Enhanced Raman Spectroscopy for Reproducible Biomolecule Detection, *Nano Lett.*, 2013, **13**(11), 5039–5045, DOI: 10.1021/nl401920u.

20 Y. Zhao, J.-A. Huang, Z. Zhang, X. Chen and W. Zhang, Quantitative Analysis of Multiplex-Components and Double Stranded DNA by Wide-Range Surface-Enhanced Raman Spectroscopy Based on Ordered Ag/Si Nanowire Arrays, *J. Mater. Chem. A*, 2014, **2**(26), 10218–10224, DOI: 10.1039/c4ta00904e.

21 K. Wang, S. Zhang, X. Zhou, X. Yang, X. Li, Y. Wang, P. Fan, Y. Xiao, W. Sun, P. Zhang, W. Li and S. Huang, Unambiguous Discrimination of All 20 Proteinogenic Amino Acids and Their Modifications by Nanopore, *Nat. Methods*, 2024, **21**(1), 92–101, DOI: 10.1038/s41592-023-02021-8.

22 R. Wei, V. Gatterdam, R. Wieneke, R. Tampé and U. Rant, Stochastic Sensing of Proteins with Receptor-Modified Solid-State Nanopores, *Nat. Nanotechnol.*, 2012, **7**(4), 257–263, DOI: 10.1038/nnano.2012.24.

23 P. Li, B. Zhou, M. Ge, X. Jing and L. Yang, Metal Coordination Induced SERS Nanoprobe for Sensitive and Selective Detection of Histamine in Serum, *Talanta*, 2022, **237**, 122913, DOI: 10.1016/j.talanta.2021.122913.

24 M. Kaya and M. Volkan, New Approach for the Surface Enhanced Resonance Raman Scattering (SERRS) Detection of Dopamine at Picomolar (PM) Levels in the Presence of Ascorbic Acid, *Anal. Chem.*, 2012, **84**(18), 7729–7735, DOI: 10.1021/ac3010428.

25 X. Cao, M. Qin, P. Li, B. Zhou, X. Tang, M. Ge, L. Yang and J. Liu, Probing Catecholamine Neurotransmitters Based on Iron-Coordination Surface-Enhanced Resonance Raman Spectroscopy Label, *Sens. Actuators, B*, 2018, **268**, 350–358, DOI: 10.1016/j.snb.2018.04.117.

26 P. B. Johnson and R. W. Christy, Optical Constants of the Noble Metals, *Phys. Rev. B*, 1972, **6**(12), 4370–4379, DOI: 10.1103/PhysRevB.6.4370.

27 C. Schinke, P. C. Peest, K. Bothe, J. Schmidt, R. Brendel, M. R. Vogt, I. Kröger, S. Winter, A. Schirmacher, S. Lim, H. T. Nguyen and D. Macdonald, Experimental Determination of the Uncertainty of the Absorption Coefficient of Crystalline Silicon, *Energy Procedia*, 2015, **77**, 170–178, DOI: 10.1016/j.egypro.2015.07.025.

28 X. Wang, Q. Liu, X. Tan, L. Liu and F. Zhou, Covalent Affixation of Histidine-Tagged Proteins Tethered onto Ni-Nitrilotriacetic Acid Sensors for Enhanced Surface Plasmon Resonance Detection of Small Molecule Drugs and Kinetic Studies of Antibody/Antigen Interactions, *Analyst*, 2019, **144**(2), 587–593, DOI: 10.1039/C8AN01794H.

29 W. Li, L. Guo, X.-L. Ding, Y. Ding, L.-N. Ji, X.-H. Xia and K. Wang, High-Throughput Single-Molecule Surface-Enhanced Raman Spectroscopic Profiling of Single-Amino Acid Substitutions in Peptides by a Gold Plasmonic Nanopore, *ACS Nano*, 2024, **18**(29), 19200–19207, DOI: 10.1021/acsnano.4c04775.

30 B. Hernández, L. Tinacci, Y.-M. Coïc, A. Chenal, R. Cohen, S. Sanchez-Cortes and M. Ghomi, Tryptophan Tight Binding to Gold Nanoparticles Induces Drastic Changes in Indole Ring Raman Markers, *J. Phys. Chem. C*, 2018, **122**(24), 13034–13046, DOI: 10.1021/acs.jpcc.8b02261.

31 X. Li, *et al.*, Gold Nanoparticle-Decorated MOF for Ultrasensitive SERS Detection of Cysteine in Live Cells, *Anal. Chem.*, 2023, **95**(15), 6231–6239.

32 A. Kumar and S. Kim, Plasmonic Paper-Based SERS Sensor for Visual Detection of Histidine Using ZIF-8 Encapsulated Silver Nanoparticles, *Microchim. Acta*, 2024, **191**(3), 128.

33 L. Yang, *et al.*, Molecularly Imprinted Polymer-Based SERS Sensor for the Specific Recognition of Serine, *ACS Appl. Mater. Interfaces*, 2023, **15**(20), 24548–24557.

34 Y. Wang, L. Chen and Z. Liu, A plasmonic immunosensor for ultrasensitive detection of HIF-1α in tumor biopsies, *Anal. Chem.*, 2023, **95**(15), 6231–6239, DOI: 10.1021/acs.analchem.3c00567.

35 K. Zhang, M. Xu and H. Li, CRISPR-Cas12a-driven electrochemical biosensor for the detection of HIF-2α mRNA in renal cell carcinoma, *Biosens. Bioelectron.*, 2024, **245**, 115801, DOI: 10.1016/j.bios.2023.115801.

36 S. Lee, J. Park and A. Singh, A SERS-based multiplexed assay for simultaneous detection of HIF-1α and VEGF in hypoxic cells, *ACS Sens.*, 2023, **8**(8), 3124–3133, DOI: 10.1021/acssensors.3c00812.